

# Modeling Material Property Heterogeneity in Fiber-Reinforced Injection Molded Plastic Parts

Kishore Pochiraju and Vojin Jovanović

*Design and Manufacturing Institute and Department of Mechanical Engineering, Stevens Institute of Technology, Hoboken, New Jersey 07030*

**Fiber reinforced plastic parts manufactured by injection molding have heterogeneous stiffness and strength behavior due to the molding process influence on the fiber orientations. This paper presents a methodology for determining the process-dependent anisotropic and inhomogeneous mechanical properties of injection-molded parts using a thickness-wise layered homogenization technique. This technique produces an equivalent laminated meso-scale representation at any location in the part and enables point-wise application of the existing laminated plate and shell theories. The methodology is demonstrated by illustrating property variations in edge-gated and center-gated plaques. Spatial variations of elastic moduli, shear modulus, and Poisson's ratio are modeled. The model can be conveniently embedded within finite element structural analyses accounting for the process-dependent material heterogeneities within the structure. POLYM. COMPOS., 26:98–113, 2005. © 2004 Society of Plastics Engineers**

## INTRODUCTION

Effective design of injection molded parts and components with fiber-filled thermoplastic materials can only be accomplished by considering the interactions between the geometry, manufacturing process, material behavior, and the mechanical performance of the part. A crucial step in predicting the part performance is the determination of the fiber orientations and prediction of the elastic behavior. The mechanical behavior of short fiber reinforced thermoplastics has been studied in the past with fiber orientation models and lamination theories. However, analyses on long-fiber (when the fiber length is more than the critical shear-lag load-transfer zone size) reinforced parts plastics are limited. The morphological characteristics (the fiber length distribution and the fiber orientation distribution) can vary markedly from position to position within a part. This will result

in anisotropic as well as inhomogeneous material stiffness and strength [1, 2]. Studies on obtaining meso-scale representations from seemingly random fiber orientation distributions are limited.

Research on modeling the flow and freezing phenomenon, fiber orientation prediction, and material property determination has met with considerable success concurrent with the advances in desktop computing. Flow and cooling phenomenon within a mold have been simulated with varying degrees of approximations [3, 4]. Crochet et al. [5] summarized that exact simulations of the flow fields and fiber orientations in an injection mold are often hampered by the lack of proper rheological models [6] and fiber orientation models that account for various interactions between the fibers and fiber-mold wall interactions. Whelan et al. [7] discussed various issues related to injection molding fiber-filled composites and parameters controlling the molding process. Advani and Tucker [3] determined fiber orientations using distribution functions and discussed the effectiveness of such a model in predicting actual distributions. Bay and Tucker [8, 9] simulated the fiber orientation in a film-gated and a center-gated disk for generalized Newtonian fluids in which velocity profiles are not affected by the fiber orientations. Gupta and Wang [10] presented a methodology that combined flow simulations with fiber orientation modeling to predict elastic properties and compared them with experimental observations. Their work showed agreement between simulated and experimentally characterized elastic stiffness properties. Drastic fiber length attrition is witnessed within the molding screw even before the hot melt enters the mold [11]. Process control and measures such as preheating the screw are cited to retain the fiber length at the mold entrance. Eduljee and McCullough [12] provided a detailed study of the models and relationships for determining elastic properties from descriptions of composite microstructure. Semi-empirical models such as the Halpin-Tsai [13] model are reasonably accurate in determining layer stiffness [2]. The Hashin-Rosen [14] direct method provides effective anisotropic material tensor for layered structures. More accurate ways of determining fiber

---

*Correspondence to:* K. Pochiraju; e-mail: kpochira@stevens\_tech.edu  
Contract grant sponsor: Design and Manufacturing Institute, Stevens Institute of Technology.

V. Jovanović is now with Smith International, Inc., Houston, Texas.

DOI 10.1002/pc.20080

Published online in Wiley InterScience (www.interscience.wiley.com).

© 2004 Society of Plastics Engineers

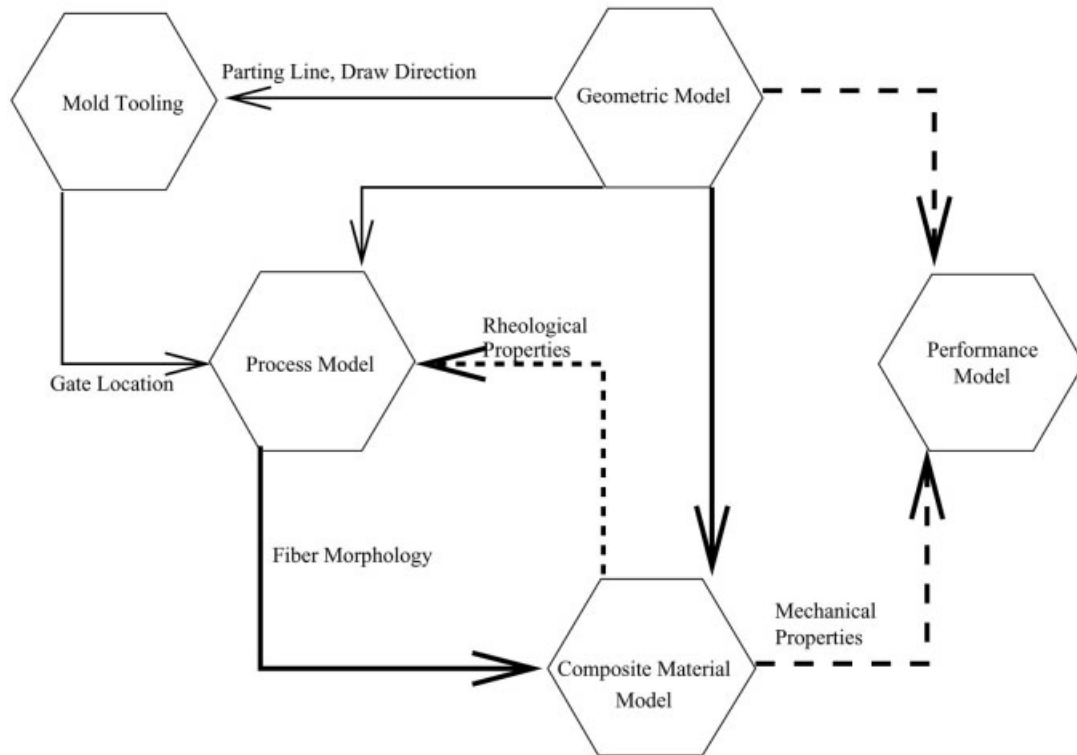


FIG. 1. Dependencies between domains affecting FRTP composite part performance.

distribution using coupled thermal and flow analysis with Jeffrey's equation are studied by VerWeyst et al. [15].

The methodology presented in this paper determines the heterogeneity and anisotropy of the elastic properties in parts molded with fiber reinforced thermoplastics. Figure 1 represents the typical dependencies between the geometry, process, material, and performance domains. The interdependencies shown in Fig. 1 as solid lines (molding, process, and material behavior) are considered. The cyclic dependency between the rheological properties of the melt on the fiber orientations is not considered.

Another assumption made in this analysis is that the part-to-part variation in the fiber morphology due to non-deterministic (stochastic) variability in the material, mold temperature profiles, and process parameters is negligible. However, these variabilities (if not suitably controlled) can affect the fiber morphology. The methodology presented here can form the deterministic simulation core of a Monte Carlo simulation to study the influence of the parameter variability on the fiber morphology, but such analysis can be significantly burdensome computationally and is considered beyond the scope of this work.

## HETEROGENEOUS MATERIAL BEHAVIOR MODEL

The material behavior is modeled using the following steps (Fig. 2):

1. The injection molding process is simulated (coupled flow and thermal analysis) which is followed by post-processing the flow data for obtaining the fiber orientation distributions.
2. Optimal parameters for the thickness-wise lamination model (layer thicknesses and effective fiber orientations within each layer) are obtained from the fiber orientation distributions.
3. The stiffness and strength behavior of the material is obtained from the fiber and matrix constituents and the layered mesostructure obtained in the previous step.

### Process Simulation

The injection molding process is simulated simultaneously with mold cavity filling and cooling of the plastic within the closed mold. In finite element based simulation techniques, the part geometry is discretized, fluid flow and thermal equilibrium of the melt within the part is determined, and a moving flow front is tracked as the part is filled. The melt entrance points are defined on the part representing the gates. Runner and cooling systems are modeled to simulate the local thermal characteristics of the mold tooling.

In this study, a 228.6 mm × 228.6 mm (9 in × 9 in) plaque mold is considered as an example to illustrate the methodology. The geometry and the coordinate system for this example part are shown in Fig. 3. Experimental work on the fiber orientation measurement [1] and elastic properties



TABLE 1. Properties of the resin.

Density ( $\rho$ )	1200 g/m <sup>3</sup>
Polymer specific heat ( $C_p$ )	1946.83 J/Kg-K
Thermal conductivity (K)	0.203475 J/m-sec-K
Viscosity model (Carreau model)	$\tau^* = 40000$ $B = .0024618, T_b = 7140$
Transition temperature ( $T_g$ )	417.15°K
Fiber weight fraction	0.5
Fiber aspect ratio ( $\alpha$ )	50
Melt temperature ( $T_m$ )	488°K
Mold temperature ( $T_{m0}$ )	316°K

$$\frac{\partial \chi}{\partial t} + V_j \frac{\partial \chi}{\partial X} = 0. \quad (8)$$

The simulation of the injection molding process is conducted using the Moldflow [16] simulation software. The thermoplastic material used in the simulations is a glass-filled polypropylene. The material properties are given in Table 1.

#### Fiber Orientation Analysis

The microstructure of the injection molded composite material is influenced by several parameters particularly the flow field of hot melt within the mold, mold temperature fields, part geometry, and part thickness. The problem of fiber-orientation determination in melt flows is well studied. Determination of the fiber orientation distributions is often carried out using computational flow and thermal models [17, 18]. Advani and Tucker [3], and later Bay and Tucker [8], described the theory of using probability distribution functions and Jeffrey's equation [19] to determine the orientation distributions of fibers during injection molding.

$$\frac{D\mathbf{a}_2}{Dt} = \dot{\omega}_{ij} \cdot \mathbf{a}_2 + \mathbf{a}_2 \cdot \dot{\omega}_{ij}^T + \lambda(\dot{\gamma}_{ij} \cdot \mathbf{a}_2 + \mathbf{a}_2 \cdot \dot{\gamma}_{ij} - 2\mathbf{a}_4 : \dot{\gamma}_{ij} + 2D_r(\mathbf{I} - 3\mathbf{a}_2)) \quad (9)$$

An averaged fiber orientation tensor describes the orientation of the fiber at any instant in the flow (Ref. 10) using a second order orientation tensor,  $\mathbf{a}_2$ . Equation 9 shows the relation between the vorticity tensor ( $\dot{\omega}_{ij}$ ) and strain rate tensor ( $\dot{\omega}_{ij}$ ). The second order orientation tensor depends on a fourth order orientation tensor,  $\mathbf{a}_4$ , which is typically written in terms of using  $\mathbf{a}_2$  with the help of a hybrid closure function. (For more details, see Refs. 3, 8, or 20).

If  $a$  and  $b$  are major and minor radii of the ellipsoidal particle then the shear ( $\dot{\gamma}$ ) and rotational components ( $\dot{\omega}$ ) of the strain tensor are given as:

$$\dot{\gamma}_{ij} = \frac{\partial V_j}{\partial X_i} + \frac{\partial V_i}{\partial X_j} \quad \dot{\omega}_{ij} = \frac{\partial V_j}{\partial X_i} - \frac{\partial V_i}{\partial X_j} \quad (10)$$

$$\lambda = \frac{(ab)^2 - 1}{(ab)^2 + 1}. \quad (11)$$

The rotary diffusivity  $D_r$ , is typically approximated [21] using an interaction coefficient,  $C_I$ ,

$$D_r = C_I \dot{\gamma}. \quad (12)$$

The appropriate value for  $C_I$  to model fiber interaction is of debate and Ref. 15 focuses on the determination of this value. For this analysis we use  $C_I = 0.001$ . The typical fiber orientation analysis output is shown at different computational layers for the molded plaque shown in Fig. 3. The figure shows one of the components of the planar fiber orientation tensor,  $a_{11}$ , in the corresponding direction,  $\theta_{11}$ , such that the cross component,  $a_{12} = a_{21} = 0$ , and the other component is computed from the fact that the trace of the orientation tensor is one. These plots are representative of the orientation information shown by the process modeling software used in this effort. Note that this plot shows the value of  $a_{11}$ , which need not be the largest orientation tensor component, and the plot is on the scale of 0 to 1. Hence, a value of  $a_{11} = 0.5$  implies that  $a_{22} = 0.5$ . Therefore, random planar orientations, where every orientation angle has the same probability in the orientation distribution, are evident.

The orientation data is rescaled on a vector plot such that the length of the vector shows the probability of distribution (zero corresponding to random distributions and maximum for aligned) and the direction showing the angle with maximum probability. Figure 4 shows the orientations at different layers after the described rescaling. Four points are identified on the plaque, designated as A, B, C, and D. The orientation distributions at these points at different layers above the midplane in the plaque are shown in Fig. 4. The orientation distributions show that while the fiber orientations near the midplane of the plaque are similar, they differ considerably with those near the surface of the plaque. For example, at location A, the maximum probability of fiber orientation occurs at around  $0^\circ$  near the midplane while the maximum occurs at  $90^\circ$  near the surface.

#### Thickness-Wise Equivalent Lamination Model

A common homogenization approach, such as the one described in Ref. 10, utilizes thickness-wise homogenization for computing the elastic stiffness and thermal expansion coefficients. Also, the homogenization is based on an artificial computational layering (eleven in this case) and does not account for the physical microstructure of the composite. The physical microstructure shown by the orientation distributions in Refs. 10 and 1 resemble layered structure where the fibers near the surface are predominantly oriented in one direction and near the center in another. Any homogenization, therefore, is more rigorous if such a structure is recognized in the microstructure.

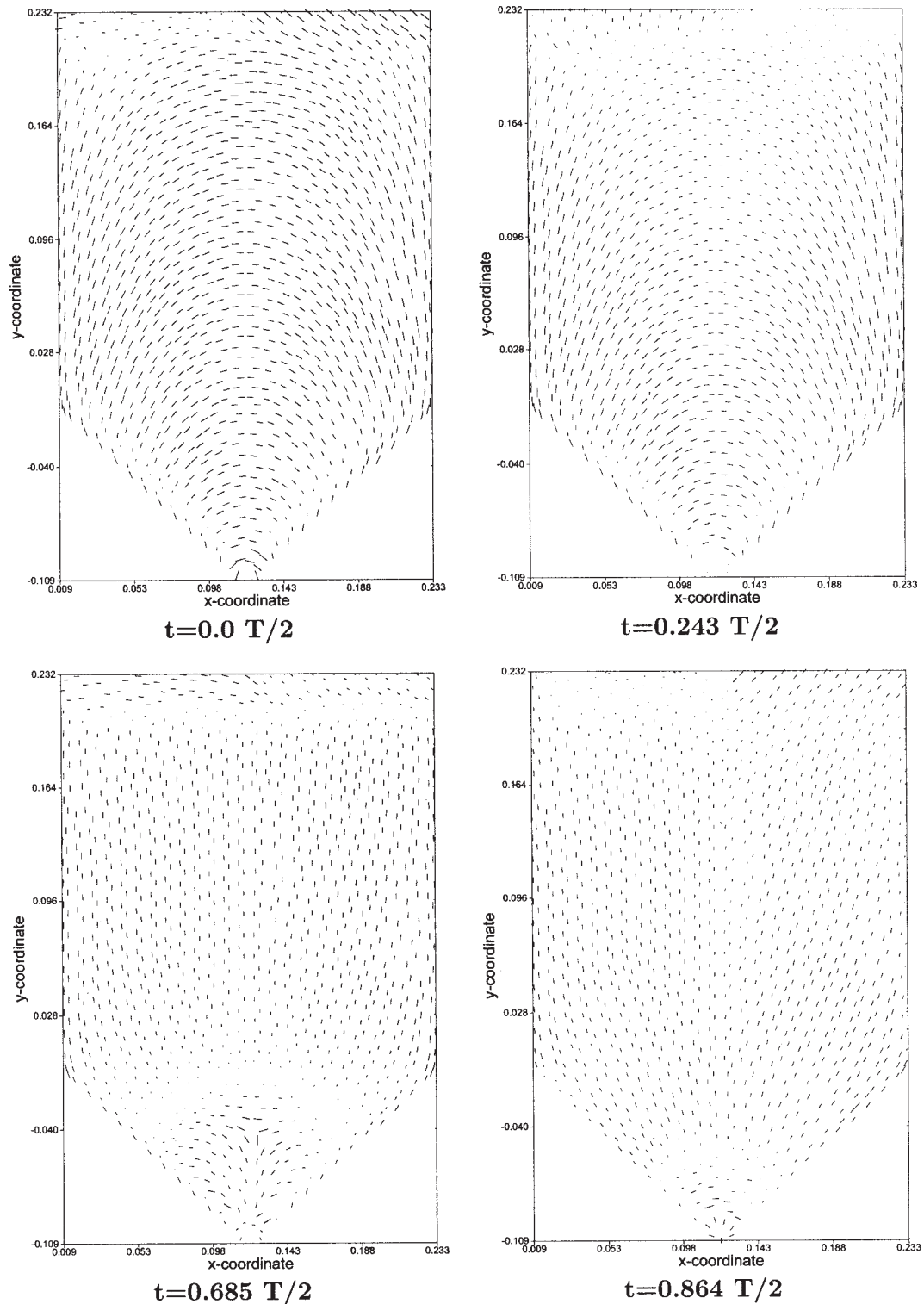


FIG. 4. Simulated fiber orientations at five layers above midplane for a plaque.

The use of a layered model to represent the fiber microstructure within an injection molded composite requires that several critical parameters be established. The orientation of the fibers within each of the layers and the volume ratio between the inner and the outer layers (shell-to-core ratio) and the characteristic fiber length are among these critical

parameters. The fiber orientation within any layer is influenced by the flow profiles with the thermal characteristics of the mold influencing the shell-to-core ratio.

For example, Fig. 4 shows clear change in the orientation distribution of the fiber (at the center of the plate) at layers  $t = 0.243 T/2$  to  $0.685 T/2$ . Recognizing at least two

TABLE 2. Orientation tensor component and direction of maximum orientation distribution ( $\theta_{11}$ ) at four locations.

Thickness position	Loc-A		Loc-B		Loc-C		Loc-D	
	$\theta_{11}$	$(\mathbf{a}_2)_{11}$	$\theta_{11}$	$(\mathbf{a}_2)_{11}$	$\theta_{11}$	$(\mathbf{a}_2)_{11}$	$\theta_{11}$	$(\mathbf{a}_2)_{11}$
0.000	179	0.882	4.13	0.834	6.52	0.825	122	0.901
0.123	179	0.819	4.24	0.806	6.63	0.809	122	0.884
0.243	179	0.65	4.56	0.718	6.89	0.763	120	0.831
0.360	178	0.297	5.61	0.516	7.51	0.655	114	0.725
0.474	91.6	0.245	16.8	0.125	9.42	0.441	100	0.611
0.583	89.8	0.565	89.3	0.475	42	0.078	84.2	0.667
0.685	88.1	0.611	90.5	0.673	91	0.518	81.1	0.717
0.779	85.7	0.602	90.7	0.703	92	0.629	80.4	0.732
0.864	82	0.553	86.5	0.644	91.3	0.694	70.9	0.709

layers for this microstructure produces two different homogenized stiffness matrices, one for the central core layer and another for the skin layer. Homogenization without this distinction provides a single anisotropic stiffness that will be an averaged value of the two layers. Experience with laminated composites shows that such a homogenization is inaccurate especially when predicting the failure modes.

The most dominant delamination failure mode cannot even be considered in the modeling without the recognition of a layered microstructure. Therefore, we formulate a methodology to determine the existence, layer thickness, and effective orientation within each layer. The methodology uses a nonlinear programming (NLP) technique and therefore the number of layers (which is an integer) are assumed a priori to eliminate the need of mixed integer non-linear programming (MINLP). Although the example shown here uses three layers, the maximum number of layers is restricted by the number of collocation points in the numerical analyses for fiber orientation and the computational resources.

The thickness-wise layering methodology entails using the fiber orientation distributions to determine the optimal number of layers (which are assumed in this case to be three—two shell layers and a core layer), a thickness of each layer ( $T_s$ ,  $T_c$ ), and the effective orientation in each layer ( $\theta_s$  and  $\theta_c$ ). The quality of the solution depends upon the number and positioning of thickness-wise collocation points in the process modeling and fiber orientation. A finite element mesh is utilized to determine the spatial variation of the fiber orientation throughout the part. The analysis described here is carried out at every integration point.

The fiber orientation analysis determines  $\mathbf{a}_2$  at several computational layers above the midplane of the part. The output is in terms of the tensor orientation data about a principal axis at every integration point on a finite element grid. Table 2 shows the  $a_{11}$  component of the edge-gated plaque at four different locations (Fig. 3). At several locations above the midsurface of the finite element, the table shows the magnitude and the orientation direction with maximum distribution probability,  $a_{11}$  and  $\theta_{11}$ , respectively. The thickness position, 0.0, corresponds to the midplane of the plaque. It is clear from this table that a three-

TABLE 3. Parameters for the layered meso-scale model.

Volume fraction	$V_f$
Fiber aspect ratio	$\alpha = l/d$
Core fraction	$T_c$
Effective core orientation	$\theta_c$
Effective shell orientation	$\theta_s$

layer, shell-core-shell structure exists for these process conditions. This drives the three layer assumption and eliminates the computational burden of MINLP to determine the effective number of layers. The objective now becomes determining the effective orientations in the shell/core layers and the layer thickness. For this we use an NLP error minimization technique. The parameters required for the using the three-layer model (Table 3) are obtained from the simulation output using an error function.

The three-layer model assumes a constant effective orientation,  $\theta_s$  or  $\theta_c$  (albeit these parameters have unknown values at this stage), in each of the three layers. This is equivalent to setting the value of  $\mathbf{a}_2$  such that the effective orientation angle is either  $\theta_s$  or  $\theta_c$ . In the tensor orientation representation scheme, such orientations at any point are characterized by  $(\mathbf{a}_2)_{11} = 1$  or  $(\mathbf{a}_2)_{22} = 0$  and the principal direction corresponds to the layer orientation.

$$\mathbf{p} = \cos \theta \mathbf{i} + \sin \theta \mathbf{j} \quad (13)$$

$$b'_{ij} = (\mathbf{a}_2)_{ij} - \frac{1}{2} \delta_{ij} \quad (14)$$

$$f'_{ij}(p) = p_i p_j - \frac{1}{2} \delta_{ij} \quad (15)$$

$$f(\mathbf{p}, \mathbf{a}_2) = \frac{1}{2 * \pi} + \frac{2}{\pi} b'_{ij} f'_{ij}(p) + O(\mathbf{a}_4) + \dots \quad (16)$$

We now define the fiber orientation distribution function,  $f(\mathbf{p})$ , for planar orientations which provide the value of the distribution function from both the simulation results and with the ideal three-layer structure with the unknown effective orientations.  $\theta$  (in Eq. 13) is any angle and  $\mathbf{i}$  and  $\mathbf{j}$  represent the unit vectors of the reference axis about which  $\theta$  is measured.

$$\text{Error}(tc, \theta_c, \theta_s) = \sqrt{\sum_{t=0}^1 \sum_{i=0}^N (f_p^{l3}(\pi i/N) - f_p^{sim}(\pi i/N))^2}$$

$$f_p^{l3}(\theta_i) = \begin{cases} \text{if } t > tc & f_p^{l3} = f(\mathbf{p}, \mathbf{a}_2 = 1 @ \theta^* = \theta_s) \\ \text{if } t < tc & f_p^{l3} = f(\mathbf{p}, \mathbf{a}_2 = 1 @ \theta^* = \theta_c) \end{cases} \quad (17)$$

$$f_p^{sim}(\theta_i) = f_p^{sim}(\mathbf{p}, \mathbf{a}_2^{sim}). \quad (18)$$

An error function, Error(), is defined as the root-mean-

TABLE 4. Microstructural parameters determined through error minimization.

Location	$T_c$	$\theta_c$	$\theta_s$
A	0.47	0.00	86.20
B	0.36	4.31	102.27
C	0.36	6.62	130.67
D	0.58	120.37	78.09

square difference between the value of the fiber orientation distribution function as obtained from the process modeling computed by the process simulation and the fiber orientation distributions expected by the three-layer model. Using a  $1^\circ$  step (i.e.,  $N = 180$ ), the values of the fiber orientation distribution function are obtained using the simulation results (using  $\mathbf{a}_2$  from simulation) and those idealized from the three-layer model. Equation 17 shows the error function used in this analysis. The function compares the orientation distributions obtained from the process modeling with the corresponding ones from the three-layer model. The orientation distribution functions  $f_p^{l3}$  are for the three-layer model while  $f_p^{sim}$  corresponds to that obtained from the simulation. The orientation distribution functions for the three-layer model are determined with an aligned orientation tensor (i.e.,  $\mathbf{a}_2 = 1$ ) and with the orientation at which the distribution function is maximum,  $\theta_*$  being either the skin orientation ( $\theta_s$ ) or the core orientation ( $\theta_c$ ). The position vector ( $\mathbf{p}$ ) is determined from the orientation angle ( $\theta$ ) using Eq. 13. The problem of estimating the parameters of the three-layer model is now posed as an unconstrained minimization problem. The microstructural variables,  $t_c$ ,  $\theta_c$ , and  $\theta_s$ , are varied as independent variables in the minimization procedure, and those values minimizing the error function (Eq. 17) are obtained. A sequential quadratic programming technique is utilized to determine the best-fit microstructural parameters. The sequential quadratic programming method as implemented by FSQP [22] was computationally less intensive and was found to converge to local minima and produce convergent estimates for the microstructural parameters. The minimization procedure took approximately 30 seconds of CPU time on a Digital Alpha work station 3000/300 for each point.

The results produced by the FSQP algorithm for microstructural parameters at the four locations on the plaque are shown in Table 4. The core ratio is higher at the center of the plaque and the effective orientations are nearly perpendicular to each other matching the in-flow and cross-flow directions. The orientations are closer to each other towards the edge of the plaque representing more aligned fiber distributions throughout the thickness of the plaque. Earlier experimental investigations [1, 2] using the process parameters simulated in this paper show that the skin core ratios vary between 20–40% of the thickness and compare well with the predictions given in Table 5.

TABLE 5. Elastic properties predicted at various locations.

Location	$E_{xx}$	$E_{yy}$	$E_{zz}$	$G_{xz}$	$G_{zy}$	$G_{xy}$	$\nu_{xy}$	$\nu_{yz}$	$\nu_{zx}$
A	7.73	6.19	4.20	3.71	2.00	2.82	0.24	0.56	0.68
B	7.73	6.21	4.20	3.71	2.08	2.76	0.24	0.57	0.68
C	9.03	5.26	4.22	3.23	1.89	3.63	0.21	0.57	0.85
D	5.15	9.38	4.22	2.90	3.73	2.19	0.086	0.87	0.63

### Stiffness Modeling for the Layered Structure

The material property model is based on a layered structure in which each layer contains fibers oriented in a characteristic direction. This reduces the number of microstructural parameters and also helps identify existence characteristic morphologies, such as a shell/core structure. A 3-D anisotropic stiffness matrix is determined based on layer thickness and characteristic orientations within each layer. Since a layer microstructure is determined from fiber orientation analysis, the present approach is equally applicable if classical laminate plate theories are used.

The injection molded composite is modeled as a three lamina symmetric structure with different properties as shown in Fig. 5. The fiber volume fraction is assumed to be constant and homogeneous through the part. A characteristic orientation of the fiber is identified in the shell layer ( $\theta_c$ ) as well as in the core layer ( $\theta_s$ ). The relative percentage of shell and core across the thickness is termed as the core ratio ( $t_s$ ). The input parameters for the three-layer model are summarized in Table 4.

The stiffness of any layer of the composite is evaluated from the characteristic fiber length and the orientation of the fiber with respect to reference axis. Halpin-Tsai relationships (Eq. 19) are used to determine the elastic stiffness for each of the layers. The stiffness of each of the layers is then transformed to the reference axes. The Halpin-Tsai relationships for determining the effective transversely isotropic material properties are given as follows:

$$E_{11} = \frac{1 + 2(l_f/d_f)\eta_L\nu_f}{1 - \eta_L\nu_f} E_m \quad E_{22} = E_{33} = \frac{1 + 2\eta_T\nu_f}{1 - \eta_T\nu_f} E_m$$

$$G_{12} = G_{31} = \frac{1 + 2\eta_G\nu_f}{1 - \eta_G\nu_f} E_m$$

$$\nu_{12} = \nu_{31} = \nu_f V_f + \nu_m V_m \quad \nu_{23} = \nu_m \quad (19)$$

$$\eta_L = \frac{\frac{E_f}{E_m} - 1}{\frac{E_f}{E_m} + 2 \frac{l_f}{d_f}} \quad \eta_T = \frac{\frac{E_f}{E_m} - 1}{\frac{E_f}{E_m} + 2} \quad \eta_L = \frac{\frac{G_f}{G_m} - 1}{\frac{G_f}{G_m} + 1} \quad (20)$$

Several different models can be employed to determine the effective macroscopic elastic properties of the composite. Classical laminated plate theories and effective homogeneous anisotropic material approximations are the two appropriate choices for modeling the material

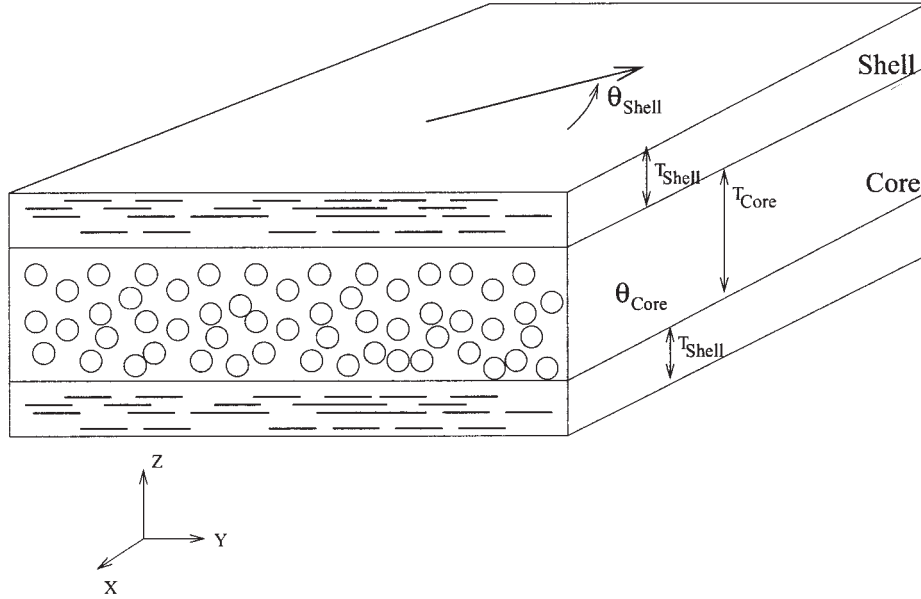


FIG. 5. Schematic of the three-layer model.

properties. In this paper, the material is considered as a homogeneous and anisotropic continuum and the properties of the composite are determined via a combination stiffness and compliance averaging. The determination of the characteristics orientation for the shell and the core layers is crucial for layered structure models to be reasonably accurate. If these parameters are determined with confidence, the layered structure representation allows the use of several mechanical models for laminates for performance analysis.

Consider the application of strain,  $\epsilon = 1$ , in the X direction to the three-layer model while the displacements of the outer surface of the body in all the other directions are constrained. Five unknowns, namely,  $C_{1i}$ ,  $i = 2 \dots 6$  in Eq. 22, can be determined using the following strain and stress relations (Eq. 21) between the layers.

$$\begin{aligned}
 \epsilon_{xx}^c &= \epsilon_{xx}^C = \epsilon_{xx}^S \\
 \epsilon_{yy}^c &= \epsilon_{yy}^C = \epsilon_{yy}^S \\
 \epsilon_{zz}^c &= \epsilon_{zz}^C(t_c) + \epsilon_{zz}^S(1 - t_c) \\
 \sigma_{xx}^c &= \sigma_{xx}^C t_c + \sigma_{xx}^S(1 - t_c) \\
 \sigma_{yy}^c &= \sigma_{yy}^C t_c + \sigma_{yy}^S(1 - t_c) \\
 \sigma_{zz}^c &= \sigma_{zz}^C = \sigma_{zz}^S.
 \end{aligned} \tag{21}$$

Using the above relationships between the stress and strain in shell and the core lamina and the averaged composite stresses and strains, the following relationships can be derived for the components of the composite stiffness matrix:

$$\begin{aligned}
 C_{11}^{eff} &= \frac{V^W}{V^S + V^W} C_{11}^W + \frac{V^S}{V^S + V^W} C_{11}^S \\
 &+ \frac{V^S V^W (C_{12}^W - C_{12}^S)^2}{(V^S + V^W)(V^S C_{12}^W - V^W C_{12}^S)} \\
 C_{12}^{eff} &= C_{12}^W - C_{22}^W \frac{V_S (C_{12}^W - C_{12}^S)}{V^S C_{22}^W + V^W C_{22}^S} \tag{22} \\
 C_{13}^{eff} &= \frac{V^W}{V^S + V^W} C_{13}^W + \frac{V^S}{V^S + V^W} C_{13}^S \\
 &+ \frac{V^S V^W (C_{12}^W - C_{12}^S)(C_{23}^W - C_{23}^S)}{(V^S + V^W)(V^S C_{12}^W - V^W C_{12}^S)}.
 \end{aligned}$$

By the application of strain along the Y axis and constraining the displacements in the remaining two axes,  $C_{22}$  can be obtained. Similarly loading along the Z direction gives  $C_{23}$  and  $C_{33}$  the following:

$$\begin{aligned}
 C_{22}^{eff} &= \frac{(V^S + V^W) C_{22}^W C_{22}^S}{V^S C_{22}^W + V^W C_{22}^S} \\
 C_{23}^{eff} &= C_{23}^W - C_{22}^W \frac{V_S (C_{12}^W - C_{12}^S)}{V^S C_{22}^W + V^W C_{22}^S} \\
 C_{33}^{eff} &= \frac{V^W}{V^S + V^W} C_{13}^W + \frac{V^S}{V^S + V^W} C_{13}^S \\
 &+ \frac{V^S V^W (C_{12}^W - C_{12}^S)(C_{23}^W - C_{23}^S)}{(V^S + V^W)(V^S C_{12}^W - V^W C_{12}^S)}. \tag{23}
 \end{aligned}$$

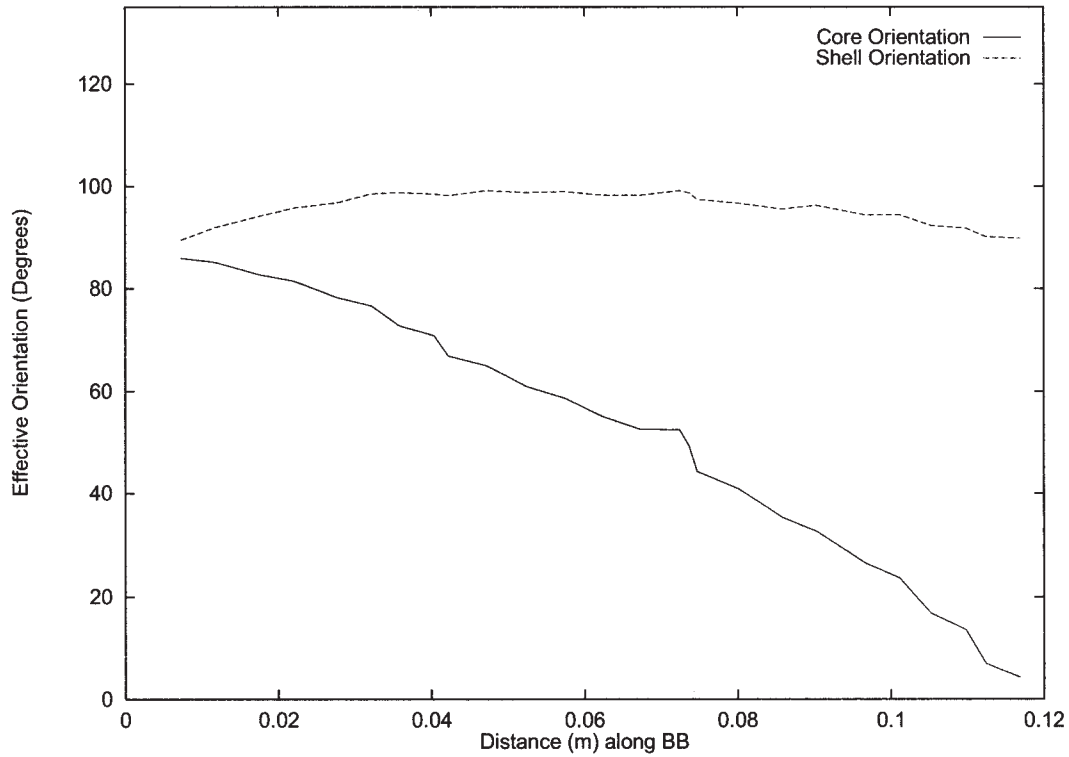


FIG. 6. Variation of the fiber orientation along the line BB.

### Modeling Strength of the Layered Structure

This layered thickness-wise method lends itself to modeling strength and failure modes using several existing theories. The strength parameters and the failure criterion can be applied at each finite element using micromechanics models for layer macroscopic strength parameters that can in turn be used in laminational models.

The strength of each layer can now be determined using micromechanics models [23] from the ultimate stress at failure values of the fiber ( $\sigma_U^f$ ), the yielding behavior of the matrix materials ( $\sigma_Y^m$ ), and the tangent stiffness ( $E_T^m$ ) in the hardening regime. For example, the transverse strength ( $S_{22}^u$ ) of a layer can be estimated [23] from the constituent properties by Eq. 24.

$$S_{22}^u = \min \left\{ \frac{\sigma_u^f - (\alpha_{e2}^f - \alpha_{p1}^f)\sigma_{22}^0}{\alpha_{p1}^f}, \frac{\sigma_u^m - (\alpha_{e2}^m - \alpha_{p1}^m)\sigma_{22}^0}{\alpha_{p1}^m} \right\} \quad (24)$$

$$\sigma_{22}^0 = \min \left\{ \frac{\sigma_Y^m}{\alpha_{e2}^m}, \frac{\sigma_U^f}{\alpha_{e2}^f} \right\} \quad (25)$$

$$\alpha_{e2}^f = \frac{E^f}{V_f E^f + 0.5(1 - V_f)(E^m + E^f)} \quad (26)$$

$$\alpha_{e2}^m = \frac{0.5(E^m + E^f)}{V_f E^f + 0.5(1 - V_f)(E^m + E^f)} \quad (27)$$

$$\alpha_{p2}^f = \frac{E^f}{V_f E^f + 0.5(1 - V_f)(E_T^m + E^f)} \quad (28)$$

$$\alpha_{p2}^m = \frac{0.5(E^m + E^f)}{V_f E^f + 0.5(1 - V_f)(E_T^m + E^f)} \quad (29)$$

Using the values for the *E*-glass fiber ( $\sigma_U^f = 3.45$  GPA with a 50–70% strength variation due to processing) and polypropylene thermoplastic matrix ( $\sigma_Y^m = 32.4$  MPa and  $E_T^m = 89.6$  MPa and a fiber volume fraction of 18%), the ply level transverse strength can be determined as 37.82 MPa. The tensile strength of unmodified 30% glass reinforced polypropylene is reported to be around 35 MPa and a flexural strength of 62 MPa (compared to the 41 MPa predicted by the above model) [24]. Similar analyses can obtain the longitudinal and the shear strengths for the layer. Then the layer strengths, the layer orientations and the layer thickness can be used with laminate failure criterion to determine the process dependent strength for the injection molded plastic part [25].

## RESULTS AND DISCUSSION

A rectangular plaque geometry is considered for analysis with two gate configurations and several inlet melt temperature conditions. The variations of the fiber orientation are shown in a series of figures. Two paths are identified in the plaque—AA (parallel to the *Y*-axis in the middle of the

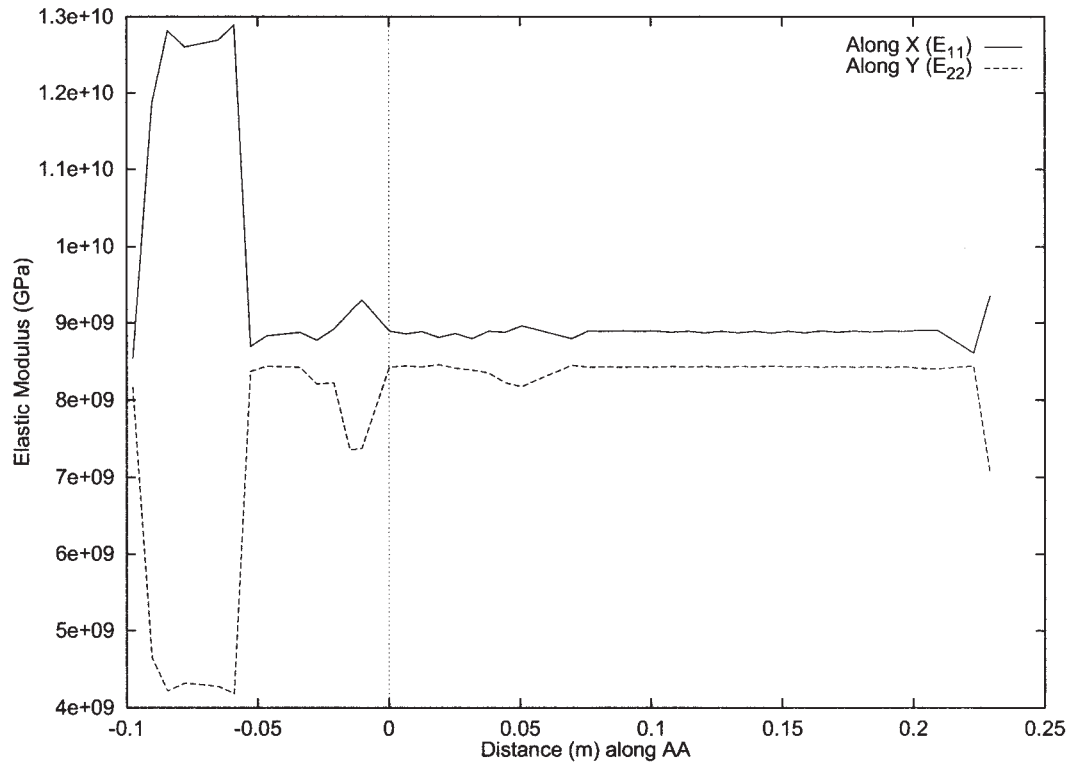


FIG. 7. Variation of the elastic moduli along the line AA.

plaque) and BB (along the  $X$  axis also in the middle of the plaque)—as shown in Fig. 3. The fiber orientation and material property variations are shown along these paths.

The results shown here are for edge-gated plaque with material and process conditions shown in Table 1. A shell-core-shell structure is evident in the square section

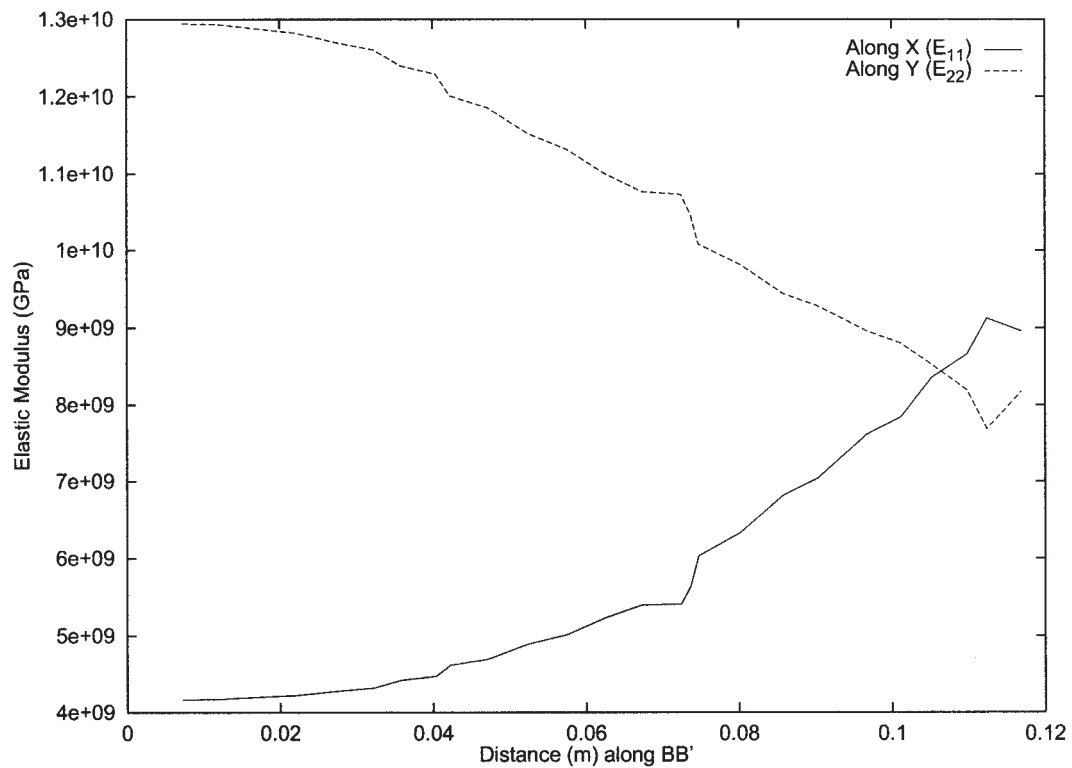


FIG. 8. Variation of the elastic moduli along the line BB.

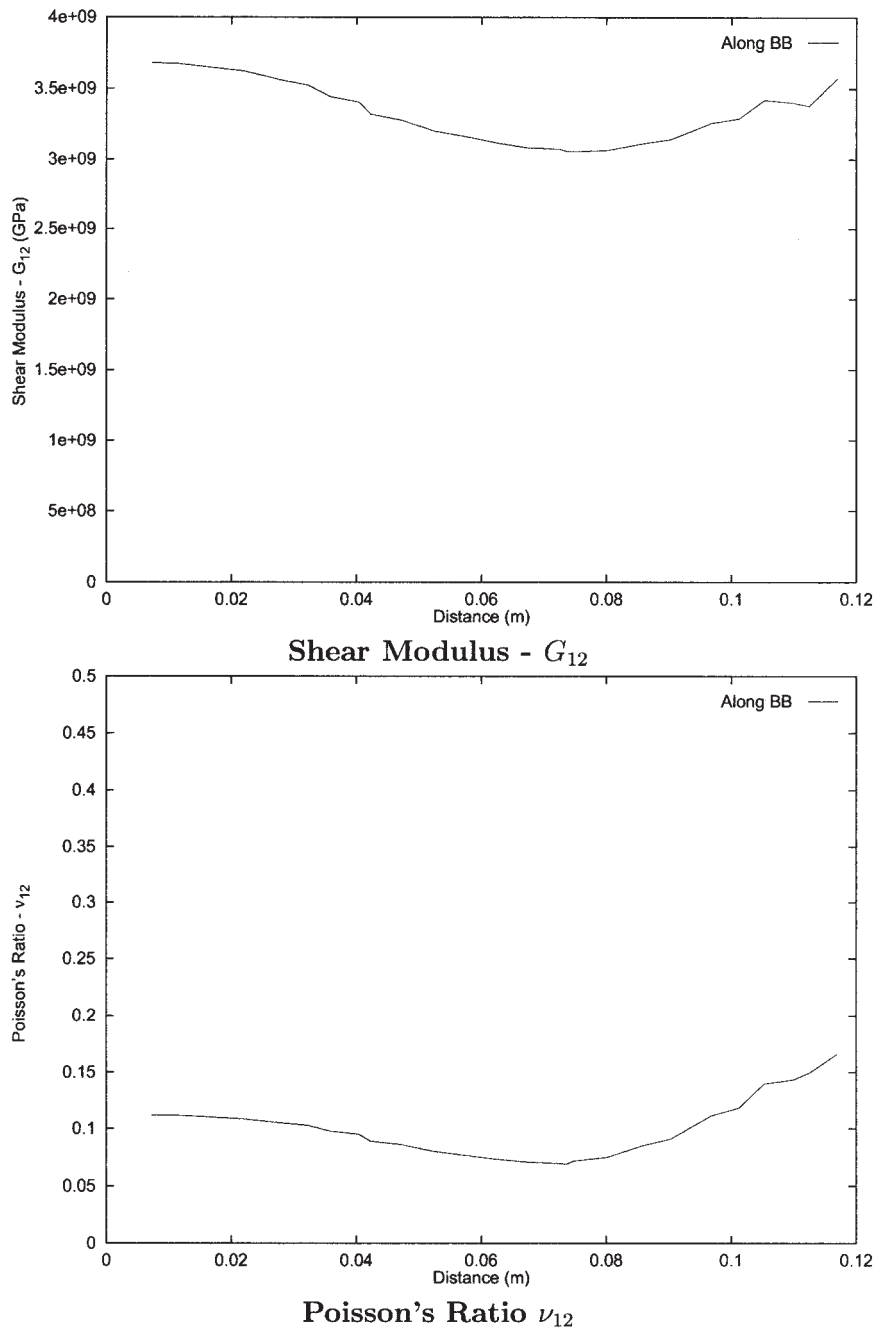


FIG. 9. Shear modulus and Poisson's ratio variation along BB.

of the plaque and the effective orientation of the fiber in the shell and core layers are shown in the figure. The core-shell ratio, core fraction ( $T_s$ ), was determined to be approximately 0.474 in the square region. The core fraction in the triangular region near the edge gate varied considerably, which is consistent with the radial nature of the flow.

Along the line BB, the fiber architecture changes from a [0/90] layered structure at the center to a 90° aligned structure at the center. This transition is shown in Fig. 6. The shell orientation is along the direction of the flow (90°) with minor variations but the core orientation varies from 0°–

90°. Therefore, the plaque is highly anisotropic at the center and becomes near quasi-isotropic in the middle. The property variations are shown in the next section.

The fiber elastic modulus and Poisson ratio are given by  $E_f = 72.5$  GPa and  $\nu_f = 0.23$ , respectively. The matrix properties are  $E_m = 2.63$  GPa and  $\nu_m = 0.38$ . With a fiber volume fraction  $V_f = 0.18$  and an aspect ratio  $\alpha = 50$ , the effective properties of the molded composite at the four locations (A, B, C, D) based on the determined microstructural parameters are given in Table 4.

Variations of the elastic moduli ( $E_{11}$  and  $E_{22}$ ) along the line AA are shown in the Fig. 7. The dotted line indicates

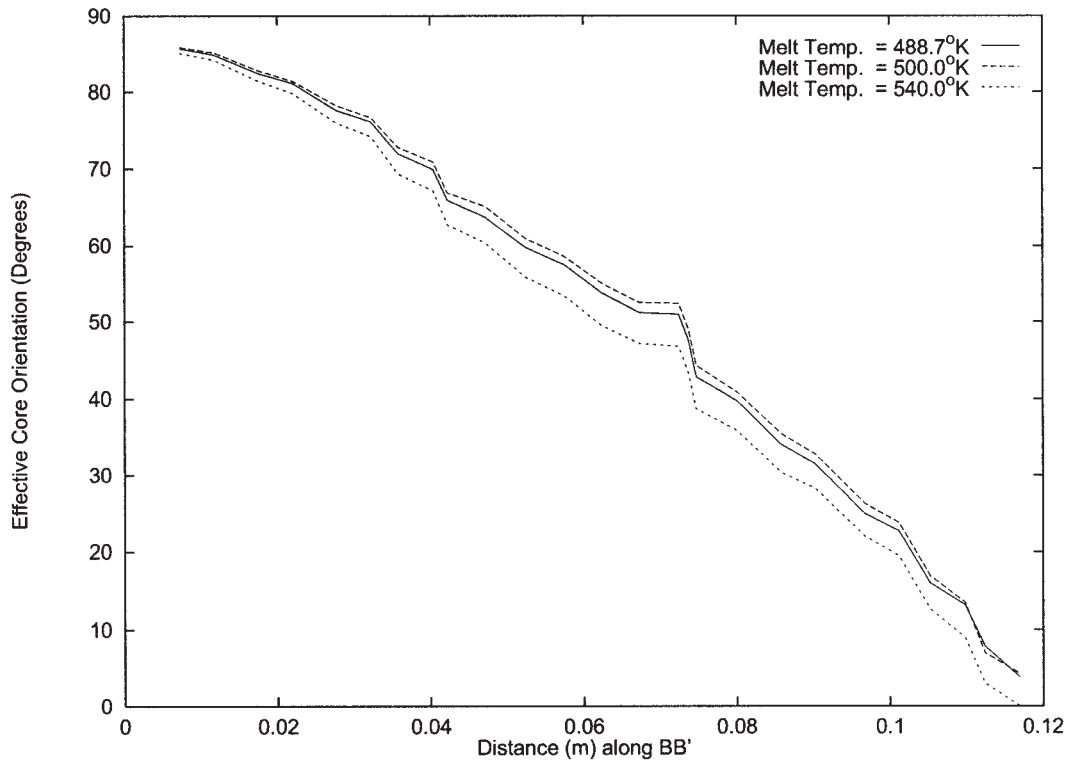


FIG. 10. Effective core orientation dependence on melt temperature.

the transition from the triangular gate region to the square section of the plaque. The square section of the plaque shows the layered structure with the elastic moduli approximately equal to each other. The accuracy of the fiber orientation prediction near the gate region is debatable due to the influence of the gate geometry and the initial fiber orientation conditions.

The elastic moduli ( $E_{11}$  and  $E_{22}$ ), the shear modulus ( $G_{12}$ ), and the Poisson's ratio variations along the line BB are shown in Figs. 8 and 9. The square section of the plaque shows the layered structure with the elastic moduli approximately equal to each other. The shear modulus is seen to be constant with variations attributed to the numerical nature of the present solution procedure. Figure 8 shows the transition from a layered structure in the middle to an aligned anisotropic structure at the edges. The moduli in the X and Y directions differ considerably with the property in the Y direction (along the flow) approaching the upper bound with the X direction modulus approaching the lower bound. The variations in the shear modulus and Poisson's ratio are shown in Fig. 9.

The effects of the inlet melt temperature and the gate location on the material heterogeneity are considered. First, the influence of varying the inlet melt temperature within an acceptable range on the material behavior is determined. The material considered, glass-filled polypropylene, has an acceptable melt temperature range of 440°–540°K. The fiber orientation variation in the core at three different melt temperatures is shown in Fig. 10.

The transition from a layered structure to an aligned structure is seen for all the three melt temperatures.

Next, a second gate location at the center of the square region of the plaque is considered. Figure 11 shows the

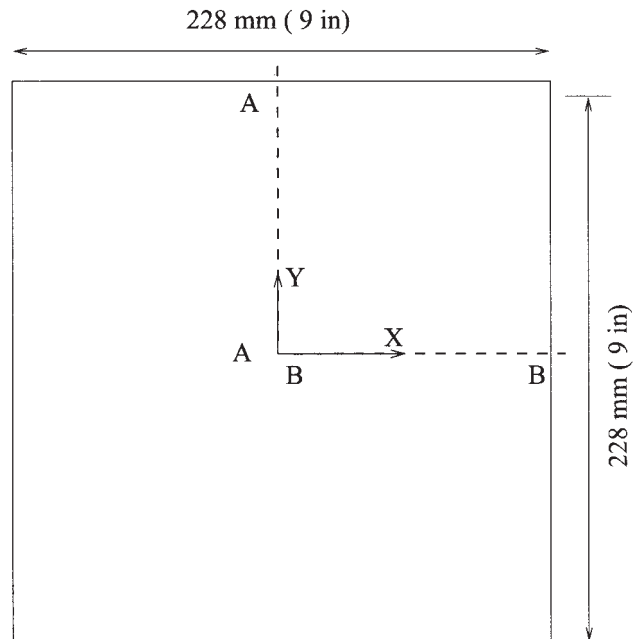


FIG. 11. Schematic of the center gate specimen and location of the coordinate systems.

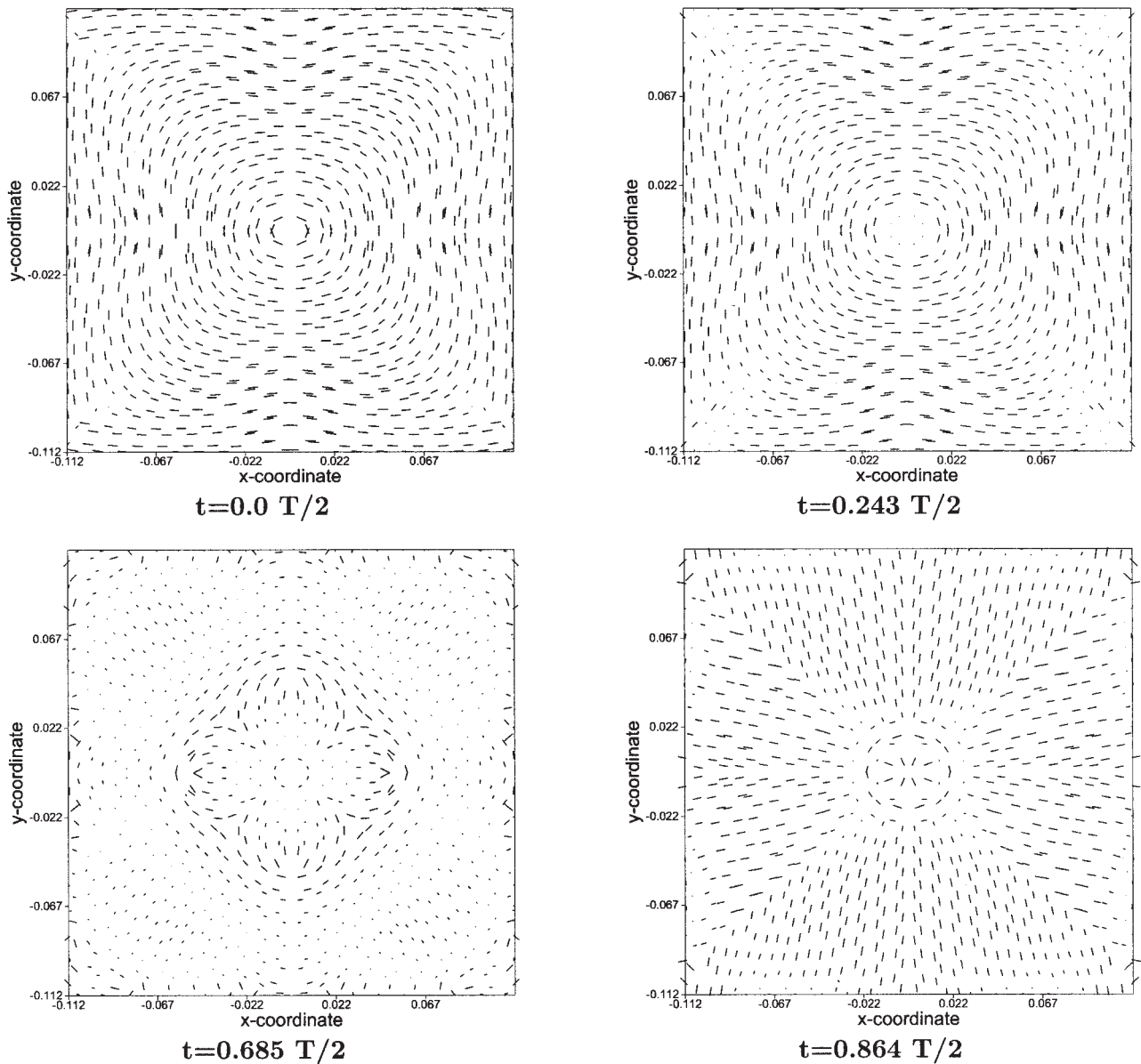


FIG. 12. Fiber orientations at four layers above midplane for center gated plaque.

location of the gate and a local coordinate system about which subsequent results are plotted.

The principal directions and the magnitude of the orientation tensor are shown at several layers in Fig. 12. This information is obtained from the process modeling and the fiber orientation analysis.

The moduli and Poisson's ratio variations are determined for both lines AA and BB. Figure 13 shows the variation of the elastic moduli along the line AA. The properties are anisotropic near the gate and represent that of a [0/90] layered structure away from the gate. The same behavior is observed along the line BB as shown in Fig. 14. The shear modulus and Poisson's ratio variations, as a function of the distance from the gate, are shown in Figs. 15 and 16, respectively. These properties indicate symmetry of the orientations and variation of the

property as a function of the distance from the gate. The simulation shows that the gate influenced the properties of the plaque to about 40 mm. After that distance, the fiber orientations stabilized to a layered structure for both the simulated configurations.

The methodology described in this paper translates the fiber orientation analysis output obtained from process modeling into a layered thickness-wise fiber morphology. The significance of fitting the layered meso-scale model from the microstructural information is that several existing models for laminated composite strength, damage progression and delamination can be used for molded plastics. The error minimization procedure computes microstructural parameters for a "best fit" laminated structure at the meso-scale.

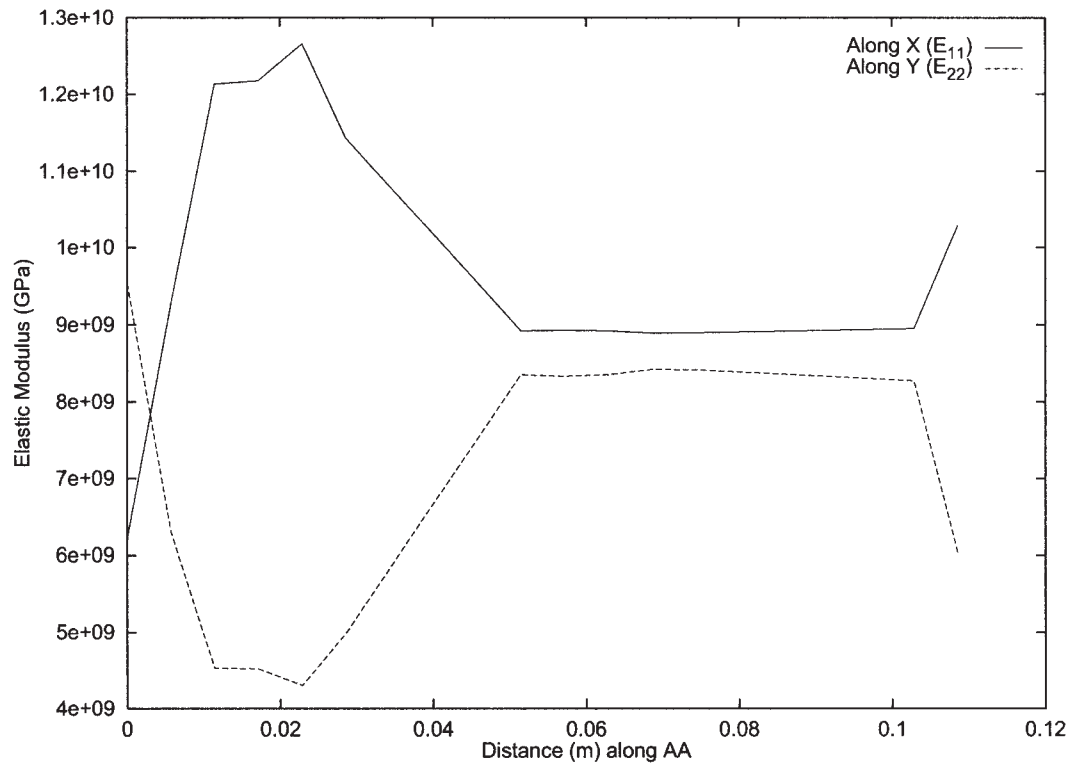


FIG. 13. Elastic moduli variation along the line AA.

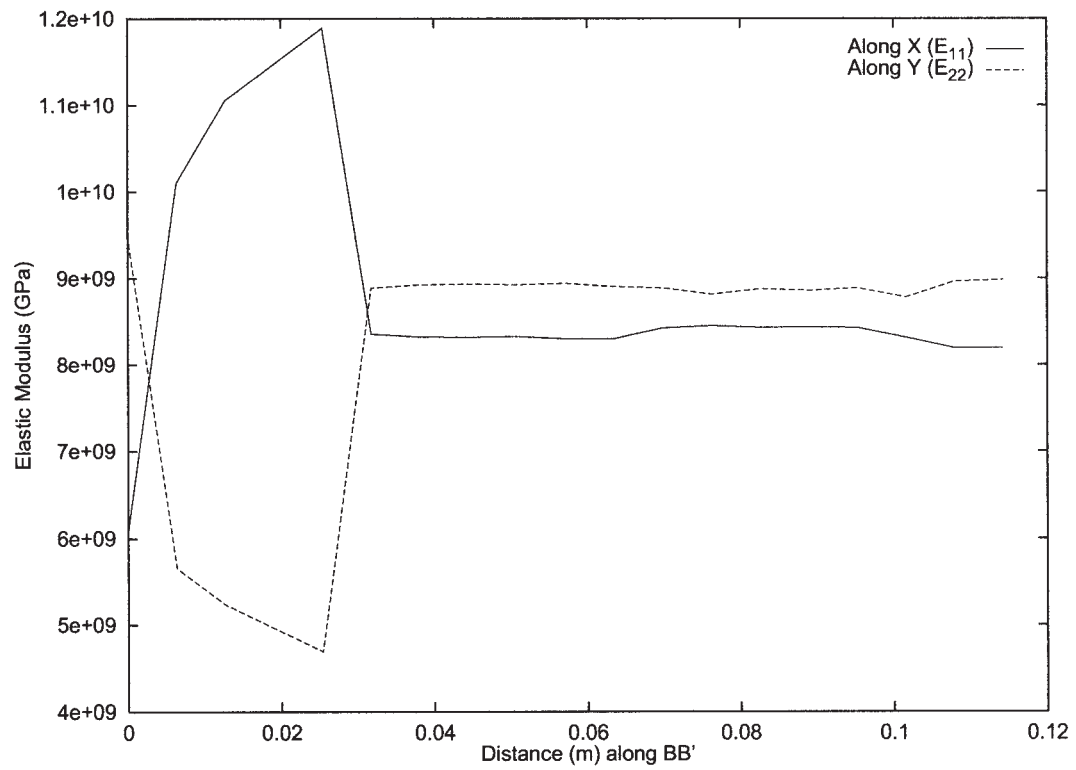


FIG. 14. Elastic moduli variation along the line BB.

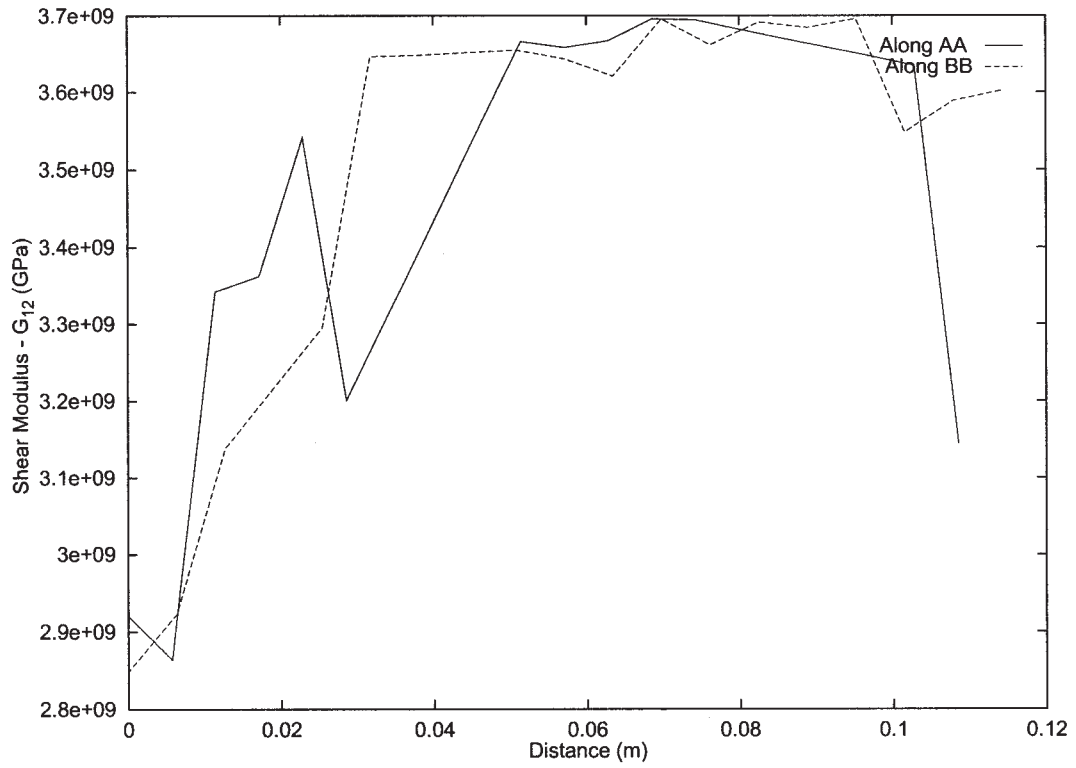


FIG. 15. Shear moduli variation for the center-gated plaque.

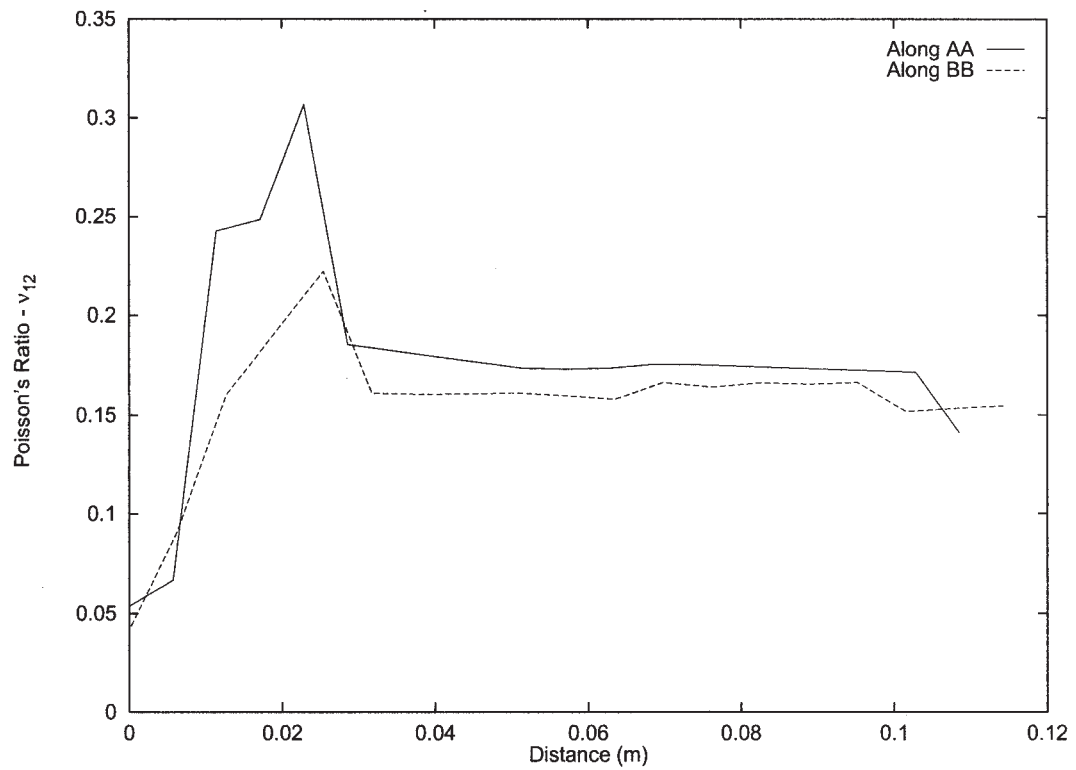


FIG. 16. Poisson's ratio variation for the center-gated plaque.

## ACKNOWLEDGMENT

The authors wish to thank Dr. Thomas Skourlis for his input on process modeling and fiber orientation analysis.

## REFERENCES

1. T. Skourlis, C. Chassapis, and S. Manoochchri, *J. Thermoplast. Compos.*, **10**, 453 (1997).
2. T. Skourlis, K. Pochiraju, C. Chassapis, and S. Manoochchri, *Compos. Part B – Eng.*, **23(3)**, 309 (1998).
3. S.G. Advani and C.L. Tucker, *J. Rheol.*, **31(8)**, 751 (1987).
4. Z. Yu, A. Ait-Kadi, and J. Brisson, *Polymer*, **35(7)**, 1409 (1994).
5. M.J. Crochet, F. Dupret, and V. Verley, “Flow and Rheology in Polymer Composites Manufacturing,” in *Composite Materials Series*, vol. 10, Chapter 11, Injection Molding, Elsevier (1994).
6. M.C. Altan, “A Review of Fiber Reinforced Injection Molding,” *J. Thermoplast. Compos.*, **3**, 275–268 (1990).
7. A. Whelan, J.L. Craft, and J.P. Goff, *Developments in Injection Molding*, vol. 1–3, Elsevier (1985).
8. R.S. Bay and C.L. Tucker, *Polym. Compos.*, **13(1)**, 317 (1992).
9. R.S. Bay and C.L. Tucker, *Polym. Compos.*, **13(1)**, 332 (1992).
10. M. Gupta and K.K. Wang, *Polym. Compos.*, **14(5)**, 367 (1993).
11. V.B. Gupta, R.K. Mittal, and P.K. Sharma, *Polym. Compos.*, **10(1)**, 16 (1989).
12. R. Eduljee and R.L. McCullough, *Delaware Composites Encyclopedia*, Technomic Publications, 381 (1993).
13. J.C. Halpin and S.W. Tsai, “Elastic Properties of Composites,” in *Technical Report AFMLTR-67-423*, U.S. Air Force (1967).
14. Z. Hashin and B. Rosen, *J. Appl. Mech.*, **31**, 233 (1964).
15. B.E. Ver Weyst, C.L. Tucker, and P.H. Foss, “Performing an Accurate Fiber Orientation Analysis,” in *ANTEC '96*, ANTEC, 726–730 (1996).
16. Moldflow Corporation, *CMOLD V96.7 Reference Manual*, Moldflow Corporation (1996).
17. P.F. Bright and M.W. Darlington, *Plastics and Rubber Processing and Application*, **1**, 139 (1981).
18. S.R. Doshi, J.M. Dealy, and J.-M. Charrier, *Polym. Eng. Sci.*, **26(7)**, 468 (1986).
19. G.B. Jeffrey, *Proc. Royal Society*, **A102**, 161 (1922).
20. G.L. Hand, *J. Fluid Mech.*, **13** (1962).
21. C.L. Tucker and F. Folger, *J. Thermoplast. Compos.*, **3**, 98–119 (1984).
22. C. Lawrence, J.L. Zhou, and A.L. Tits, *Users Guide for CFSQP Version 2.3*, University of Maryland, College Park (1993).
23. Z.M. Huang, *Mater. Lett.*, **40**, 164 (1999).
24. T.N. Novotortzeva, O.B. Kulachinckaya, M.B. Andreeva, E.B. Kalugina, I.L. Aizinson, A.S. Lunin, V.A. Tochin, Ya. G. Urman, I.G. Kalinina, K.Z. Gumargalieva, and G.E. Zaikov, *Polym. Degrad. Stabil.*, **69(1)**, 17 (2000).
25. R. F. Gibson, *Principles of Composite Material Mechanics*, McGraw-Hill Higher Education (1994).